Contents lists available at ScienceDirect

Comptes Rendus Mecanique

www.sciencedirect.com

Jet noise modelling and control / Modélisation et contrôle du bruit de jet

A diagnostic tool for jet noise using a line-source approach and implicit large-eddy simulation data

Florent Margnat [a,*], Vasilis Ioannou [b], Sylvain Laizet [b]

[a] *Institut Pprime, CNRS, Université de Poitiers, ISAE–ENSMA, 86962 Futuroscope Chasseneuil, France*
[b] *Department of Aeronautics, Imperial College London, London, SW7 2AZ, UK*

A R T I C L E   I N F O

A B S T R A C T

In this work, we propose a cost-effective approach allowing one to evaluate the acoustic field generated by a turbulent jet. A turbulence-resolving simulation of an incompressible turbulent round jet is performed for a Reynolds number equal to $460,000$ thanks to the massively parallel high-order flow solver Incompact3d. Then a formulation of Lighthill's solution is derived, using an azimuthal Fourier series expansion and a compactness assumption in the radial direction. The formulation then reduces to a line source theory, which is cost-effective to implement and evaluate. The accuracy of the radial compactness assumption, however, depends on the Strouhal number, the Mach number, the observation elevation angle, and the radial extent of the source. Preliminary results are showing that the proposed method approaches the experimental overall sound pressure level by less than 4 dB for aft emission angles below $50°$.

1. Introduction

The overall goal of the present study is to develop and validate a cost-effective hybrid jet noise prediction tool that could potentially offer a competitive trade-off between the accuracy of the experiments (in the same operating conditions) and the computational cost in terms of wall clock time and data storage. Such a tool could be critical for the efficient design of quieter turbulent jets and for quickly evaluating and comparing different noise mitigation strategies. For instance, to reduce the sound generated by aircraft engines, Boeing, General Electric, and NASA developed several years ago serrated edges called chevrons for engine exhaust nozzles [1,2]. The chevrons effectively reduce jet noise by controlling the way the air mixes after passing through and around the engine. However, the large number of parameters affecting the performance of such a control solution makes their development, testing and optimisation a very complicated task, with potentially numerous high-cost and time-consuming trial-and-error iterations. For this reason, cost-effective diagnostic tools are needed in order to quantify how the acoustic field is modified when a control solution is used, but more importantly to adjust and compare different parameters of the control solution in an effective fashion. The expectation for such a diagnostic tool may include quantitative and qualitative criteria, such as a correct estimation of the global sound levels without any empirical constant, and an ability to reveal significant changes in the directivity pattern and frequency content.

---

* Corresponding author.
E-mail addresses: florent.margnat@univ-poitiers.fr (F. Margnat), vasilis.ioannou14@imperial.ac.uk (V. Ioannou), s.laizet@imperial.ac.uk (S. Laizet).

Coupling compressible, large-eddy simulations (LES) with a wave extrapolation from a Kirchhoff surface is currently the most adopted strategy to quantify noise levels generated by turbulent jets. However, because the acoustic predictions are often carried out at the same time as the simulation, the potential for computational cost reduction is quite small. The very high cost of this direct approach, very successful to unlock the sound generation mechanisms for turbulent jets, is still a limiting factor to be used as a cost-effective diagnostic tool. Recent works have provided powerful insight into the ingredients of jet noise generation that might be helpful when trying to design a diagnostic tool. From the flow dynamic point of view, the boundary layer characteristics inside the nozzle [3] and the hydrodynamic instabilities at the initial stage of the shear layer have been identified as driving phenomena in the early stages of the development of turbulent jets [4,5]. From an acoustic point of view, the azimuthal mode decomposition of the acoustic field reveals that most of the energy is contained in the couple of first modes [6]. The near-field properties of those modes has been characterised by [7] through the streamwise evolution of instability waves. The higher modes are formally less efficient to radiate to the far-field. Another important feature of the acoustic field is its directivity, which needs an extended source to be reproduced [8], meaning that phase effects along the jet axis must be accounted for by any modelling. As for phase effects in the third direction, the transverse one, the lower the frequency and the radiation angle are, the weaker their influence is.

Taking into account all these considerations, a hybrid methodology is developed in the present study in order to evaluate sound levels generated by turbulent jets. The first step generates source data by an optimised turbulence-resolving simulation using an incompressible, massively parallel, high-order solver. The nozzle is included in the computational domain for a more realistic representation of the flow physics and an implicit large-eddy simulation (ILES) strategy is used to reach high Reynolds numbers while resolving a wide range of turbulence scales. Such a simulation can be performed in a few hours on a few thousands cores, contributing to an excellent balance between wall-clock time and accuracy. The second step is an azimuthally reduced, semi-compact formulation of Lighthill's solution: all effects are included in the axial direction, while only the five first azimuthal modes of the source quantity are propagated and a first-order compactness assumption is made in the radial direction. This leads to a line-source approach, for which the storage need and computational time are almost negligible with respect to the flow simulation.

The paper is organised as follows: in section 2, the numerical strategy for the flow simulation is described, and the velocity field is compared with experimental data [6,9,10] performed at the same Reynolds number. The acoustic methodology is presented in section 3, while the predicted acoustic field is validated in section 4 versus the experimental acoustic measurements [11] generated in the same facility as for the velocity field data. The range of validity of the radial compactness assumption is thus studied in terms of aft radiation angle and frequency. The full derivation of the present method as well as its limitations are presented in the appendix.

2. Flow simulation

The main goal of the flow simulation reported in this section is to provide the velocity field data necessary for the acoustic study.

2.1. Numerical methods

The governing equations are the forced incompressible Navier–Stokes equations

$$\frac{\partial \mathbf{u}}{\partial t} = -\nabla p - \frac{1}{2} \left[\nabla \left(\mathbf{u} \otimes \mathbf{u} \right) + (\mathbf{u} \cdot \nabla)\mathbf{u} \right] + \nu \nabla^2 \mathbf{u} + \mathbf{f} \tag{1}$$

$$\nabla \cdot \mathbf{u} = 0 \tag{2}$$

where $p(\mathbf{x}, t)$ is the pressure field (for a fluid with a constant density) and $\mathbf{u}(\mathbf{x}, t)$ the velocity field. Note that convective terms are written in the skew-symmetric form as it allows the reduction of aliasing errors while remaining energy conserving [12]. In these forced Navier–Stokes equations, the forcing field $\mathbf{f}(\mathbf{x}, t)$ is used through a customized immersed boundary method (IBM) allowing us to include the nozzle inside the computational domain. Following the work of [13], the present methodology is based on an alternating direction forcing strategy for which a no-slip boundary condition is imposed at the wall of the nozzle in each spatial direction, while an artificial flow is introduced inside the nozzle to avoid any loss of continuity on the velocity field. From a practical point of view, this artificial expansion of the flow inside the nozzle, based on Lagrange polynomials, is performed in the direction where a spatial derivative is evaluated. As a consequence, a different expansion is generated, depending on the spatial direction of the computed derivatives. When combined with low-order schemes, a loss of continuity would only have a minor impact on the solution. However, when combined with high-order schemes, it can generate spurious oscillations on the derivatives at the wall of the nozzle. More details about this technique can be found in [13].

The governing equations are solved using the flow solver `Incompact3d` based on a Cartesian mesh, finite-difference sixth-order schemes for the spatial discretization and a conventional fourth-order Adams–Bashforth scheme for the time advancement. To treat the incompressibility condition, a fractional step method requires to deal with a Poisson equation, fully solved in spectral space via the use of relevant 3D Fast Fourier transforms. Combined with the concept of modified wave number [14], this direct (i.e. non-iterative) technique allows the implementation of the divergence-free condition up to machine accuracy. A partially staggered mesh is used where the pressure mesh is shifted by a half-mesh from the velocity
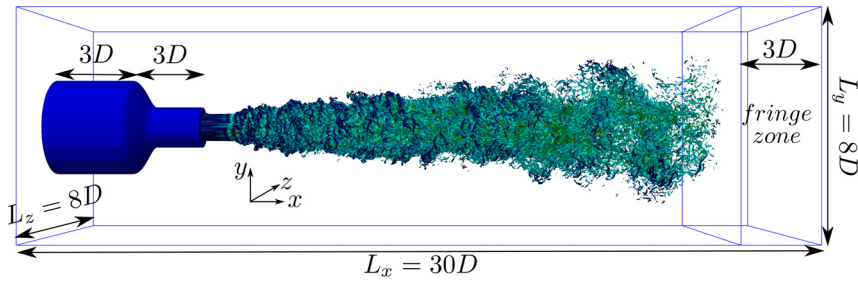
Fig. 1. Schematic diagram of the computational domain.

mesh in each direction. This type of mesh organization leads to more physically realistic pressure fields with no spurious oscillations. More details about the numerical methods used in `Incompact3d` code can be found in [15].

The high level of parallelisation in `Incompact3d` is achieved thanks to a highly scalable 2D domain decomposition library and a distributed Fast Fourier Transform (FFT) interface [16]. The 3D computational domain is divided in pencils with three different options referred as X-pencil, Y-pencil, and Z-pencil. The derivatives and interpolations in the x-direction (y-direction, z-direction) are performed in X-pencil (Y-pencil, Z-pencil), respectively. The 3D FFTs required by the Poisson solver are also broken down as series of 1D FFTs computed in one direction at a time. `Incompact3d` can scale well up to one million MPI-processes for simulations with several billion mesh nodes [16]. It has been used recently for a variety of projects[1] ranging from fractal-generated turbulence [17], gravity currents [18], boundary layers [19], impinging jets on a heated plate [20], active flow control of a turbulent jet [13,21], and simulations of plasma actuators [22].

2.2. Flow configuration

In this study, we consider a turbulent main jet at the exit of a round nozzle of internal diameter D. For better modelling of the instabilities at the exit of the nozzle, the latter is included inside the computational domain $L_x \times L_y \times L_z = 30\,D \times 8\,D \times 8\,D$, as shown in Fig. 1. It is discretized on a Cartesian mesh of $n_x \times n_y \times n_z = 1281 \times 513 \times 513$ mesh nodes and split into 2,048 computational cores. The Reynolds number is $\text{Re} = U_c D/\nu = 460,000$ where U_c is the velocity of the jet on the centerline at the exit of the nozzle. The coordinate system $\mathcal{R}$ is orthonormal with coordinate x in the streamwise direction and coordinates (y, z) in the transverse plane such that $y = z = 0$ on the centerline. The origin of $\mathcal{R}$ is located just at the exit of the nozzle on the centerline of the main jet, at a distance 6D from the upstream side of the computational domain. For the initial inlet boundary condition at $x = -6D$, the diameter of the nozzle is 3D with a velocity profile inside the nozzle based on a mean profile $U(r) = [1 - (2r/3D)^{64}]U_c$ where $r = \sqrt{y^2 + z^2}$ (corresponding to the radial coordinate). The first part of the nozzle is based on a constant diameter up to $x = -3\,D$. Then the diameter is reduced to 1D from $x = -3\,D$ to $x = -2\,D$ using the function $-9.48\,((0.75\,(x + 2.0))^4 + (0.75\,(x + 2))^3) + 0.5\,D$ to define the radius of the nozzle in the convergent part. The last part of the nozzle has a constant diameter D from $x = -2\,D$ to $x = 0$. Turbulent conditions inside the nozzle are triggered with a conventional recycling technique where the velocity profile at $x = -4.5\,D$ is used at the inlet, see [23] for more details. Note that no rescaling and no interpolation are necessary as the diameter of the nozzle is constant in the recycling region. The velocity around the nozzle is not zero with the imposition of a small co-flow of velocity equal to $4\%\,U_c$. This co-flow avoids dealing with a stagnant flow near the outlet, a situation that is very critical for any outflow boundary conditions in incompressible flows. In order to ensure the no-slip boundary condition for the outside wall of the nozzle, a laminar boundary profile is imposed with a thickness of about 9 meshes. The experimental nozzle boundary layer exit thickness is not known, as it is extremely difficult to measure. However, it was estimated to be approximately $0.08\,D$ [3]. For our simulation, the nozzle boundary layer exit thickness is approximately equal to $0.07\,D$, which is very close to the estimated experimental value.

At the end of the domain in the streamwise direction, the fringe method proposed by [24] is implemented as the popular convective open boundary condition is unsuitable [25]. This technique consists in the addition of a volume force F_v in the right-hand side of the Navier–Stokes equations with $F_v = \lambda(x)(\mathbf{u}_T - \mathbf{u})$, where $\mathbf{u}_T$ is a target velocity field and $\lambda(x)$ a modulation function allowing a local activation of the forcing in the region where $\lambda(x) \neq 0$. Here, the corresponding fringe region is defined using $\lambda(x) = \cos^2\left[(x - x_{\text{exit}}) \times \dfrac{\pi}{6}\right]$, for $x \geq x_{\text{exit}}$, where x_{exit} is the x value at the exit of the regular domain, i.e. $x = 27\,D$ as seen in Fig. 1. This function is suitable due to the fact that the forcing is smoothly starting from zero (first derivative is also zero) at the exit of the regular domain and is increasing to 1 at the exit of the fringe zone. $\mathbf{u}_T$ is assumed to be of Gaussian type, with $(u_{\text{max}} - u_{\text{cf}}) \times e^{(-r^2/r_g^2)} + u_{\text{cf}}$, where u_{cf} is the velocity of the coflow and u_{max} is the velocity on the centerline of the jet. The values of $u_{\text{max}} = 0.25$ and $r_g = 1.4$ are used for the targeted velocity at the end of the physical domain (at $x = 30\,D$) as these values are matching a preliminary investigation with no fringe zone. The outflow boundary

---

[1] See http://www.incompact3d.com/impact.html for all the Incompact3d-based papers published recently.

condition (at $x = 30\,D$) is then given by a standard 1D convective open boundary condition, with a convective velocity being equal to the exit velocity at each node.

For the lateral sides ($y = \pm L_y/2$ and $z = \pm L_z/2$), modified Dirichlet boundary conditions are imposed, following a procedure described in [26]. The idea is to allow the flow to enter the computational domain in order to mimic an entrainment mechanism. Note that, in the present study, the aspiration of fluid is marginal (less than $0.01\,U_c$), with no significant impact by comparison to more classic free-slip boundary conditions.

2.3. Implicit large-eddy simulation (ILES)

Recently, [27] and [28] suggested an original method to enable the introduction of a controlled numerical dissipation restricted to a selected range of small scales. This method is based on specific high-order finite-difference schemes for the computation of the second derivatives in the viscous term of the Navier–Stokes equations. The schemes are centered so that no upwind treatment is required contrary to the popular use of non-centered dissipative schemes for the computation of first derivative in the convective terms. The dissipation can be easily controlled through the coefficients of the scheme while preserving its formal accuracy. The set of coefficients provided by [28] is designed to mimic a subgrid-scale model for LES based on the concept of Spectral Vanishing Viscosity (SVV, see, for instance, [29,30]), at no extra computational cost. The coefficients used in the present study can be found in [20] and have allowed us to reach, at a reasonable computational cost, the same Reynolds number as the experimental database used in the present study for comparison [6,9,10].

2.4. Reference data

A massive dual-plane, time-resolved, stereoscopic particle-image velocimetry (PIV) experimental database has been generated recently at the "Bruit et Vent" jet-noise facility of the Pprime Institute, Poitiers, France [6,9,10]. The measurements were carried out at a Mach number equal to 0.4 in isothermal conditions. The nozzle diameter D was 0.05 m, giving a Reynolds number of 460,000 equal to the one used in the present study. Acoustic data were also collected with a 18-microphone azimuthal array, of radius $r/D = 14.3$, whose axial position is varied so as to map the sound field on a cylindrical surface, giving access to the overall sound pressure level (OASPL) and spectrum for the 10 first azimuthal modes in addition to that of the total radiation. The axial measurement range is $-2.5 \simeq x/D \simeq 39$, thus covering an aft angle range $20° \leq \theta_o \leq 105°$ with a constant increment of $5°$. On account of the resulting differences in the distance R_o, between the nozzle exit and the microphones, a $1/R_o$ scaling is applied to the acoustic pressure in order to rescale the measurements to a fixed distance of $R_o = 42\,D$, which corresponds to a maximum on the cylindrical surface, namely for $\theta_o = 20°$. This scale is not fully justified for low frequencies; however, the conclusions of the present numerical study were found unchanged when the comparison with the experimental data was taken on the cylindrical array. The acoustic intensity is also scaled by M^4 to account for changes in the dynamic head of the jet and to ease the comparison with simulations.

2.5. Incompressible ILES results

Fig. 2 is showing an instantaneous visualization of the flow just at the exit of the nozzle. As expected, it can be seen that the jet is fully turbulent, with a wide range of vortices. It seems that it is not possible to identify small-scale spurious numerical oscillations, which our simulations would have been unable to control. A short transitional period can be observed just at the exit of the nozzle followed by large-scale ring structures that are generated close to the nozzle. Those structures are quickly destroyed by small streamwise vortices due to the Kelvin–Helmholtz instability mechanism, and eventually the flow becomes gradually fully turbulent.

Fig. 3 shows a comparison of the streamwise velocity statistics from the experimental database and from the present simulation at various streamwise locations downstream of the nozzle exit, from $x = 3\,D$ to $x = 8\,D$. For this figure, the data are averaged azimuthally to improve the statistical convergence. It can be seen that a reasonably good agreement is obtained between the experiment and the simulation for the streamwise evolution of the mean streamwise velocity and its associated fluctuating component. The small differences observed for the fluctuating component are attributed to the co-flow that could affect the entrainment process. Also, it has been shown recently that the nature of the boundary layer inside the nozzle is a crucial parameter allowing us to reproduce experimental data at high Reynolds numbers [3]. In this study, the authors used localized adaptive mesh refinement, synthetic turbulence, and wall modeling inside a convergent nozzle to ensure realistic turbulent boundary layer profiles inside the nozzle. The turbulent structures generated by our recycling technique may not be realistic enough for a correct reproduction of the levels of turbulence generated experimentally downstream of the nozzle exit. Finally, the present simulation is incompressible, whereas the experiments were performed at $M = 0.4$. Compressibility effects, which cannot be taken into account in the simulation, could affect the streamwise evolution of the jet. In the simulation, the length of the potential core is $5.3\,D$, in very good agreement with the experimental data, for which the potential core is estimated to be between $5\,D$ and $5.5\,D$ [9].

For completeness, streamwise velocity spectra on the jet centerline (left) and the jet lipline (right) at a distance of 2D after the nozzle exit are plotted in Fig. 4. It can be seen that the agreement between the experimental data of [9,10] and the present numerical data is quite good on the jet lipline, where a clear $-5/3$ spectra can be observed for a fairly large range of Strouhal numbers, with no distinctive peak. On the jet centerline, a major difference can be observed between the
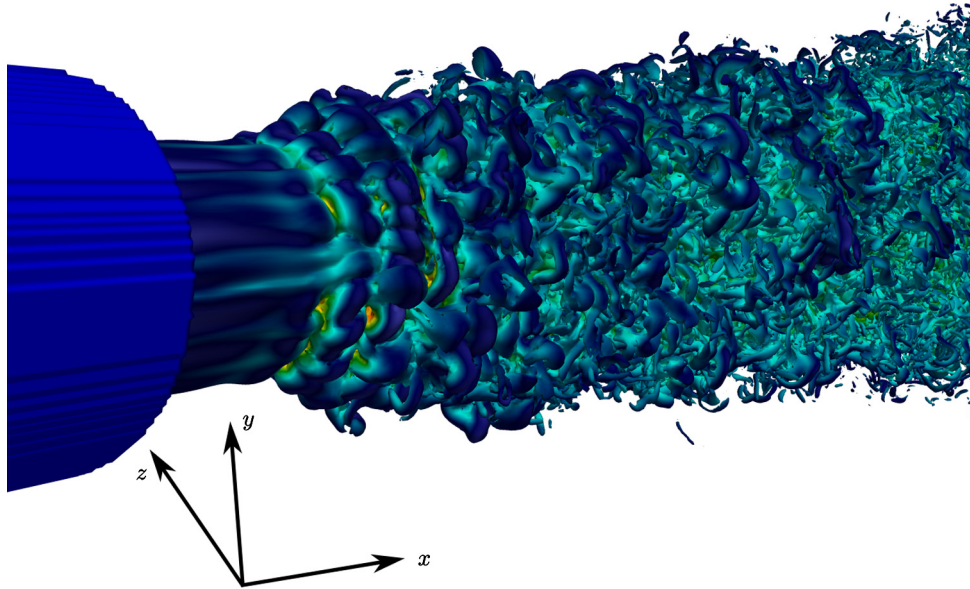
Fig. 2. Instantaneous visualization of the flow downstream of the nozzle exit. Isocontour 10 U_c/D^2 of enstrophy coloured by the streamwise velocity (dark blue corresponds to zero and red corresponds to 1).
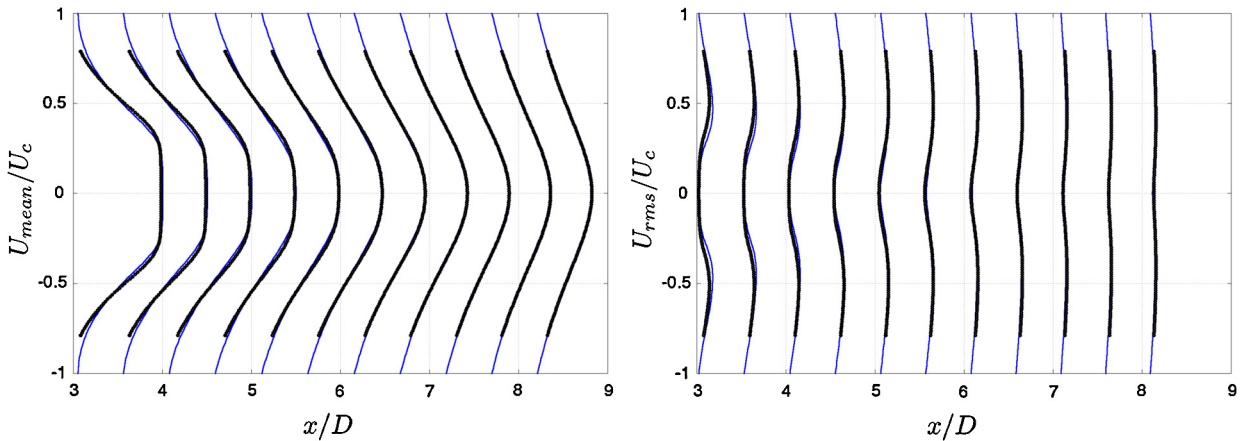

Fig. 3. Profiles for the mean streamwise velocity and its associated fluctuating component for $x/D = 3$ to 8. Comparison between our ILES (blue lines) and the experimental data of [9,10] (black symbols).

experimental data and the present simulation. In particular, the location of the peak is different at low Strouhal numbers, being equal to 0.3 for the simulation and to 0.6 for the experiments. As explained in [9], the centerline spectrum is expected to be representative of the axisymmetric mode, which is the case for the experiments. However, it seems that for the simulation, the peak corresponds to the preferred jet column mode ($St = 0.3$), see [31,32]. This difference in the location of the peak is attributed to the recirculation mechanism used in the nozzle to trigger instabilities inside the boundary layer. By triggering instabilities at a frequency corresponding to the axisymmetric mode, it should be possible to shift to the right the peak observed on the streamwise velocity spectra on the jet centerline.

To conclude, even if the agreement with the experiments is not that great, the incompressible data can be used (as a first try) for the acoustic study in order to assess the feasibility of the cost-effective diagnostic tool.

3. Acoustic methodology

Using the velocity field from the simulation described above, the jet noise prediction consists of a line-source approach based on three steps. Starting from incompressible velocity fields, an analogy is needed to build the acoustic source. Lighthill's theory of aerodynamic noise [33] is used here for its simplicity of formulation and implementation [34–38]. Secondly, following the ring model [39,40] the source field is decomposed into a Fourier series in the azimuthal direction, which is homogeneous. This is a very efficient way to compress the data [41] and the acoustic computation time, since
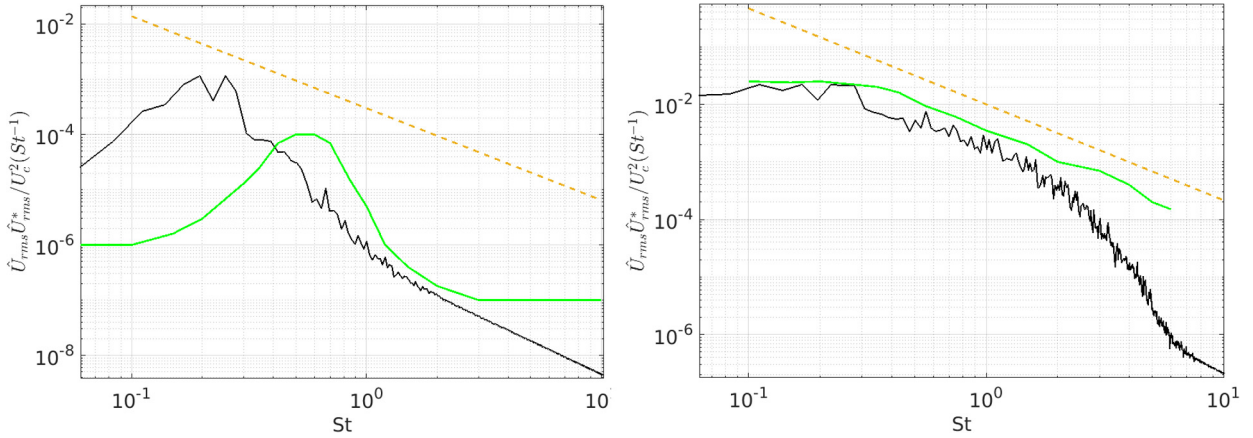
Fig. 4. Streamwise velocity spectra on the jet centerline (left) and the jet lipline (right) at a distance of 2D after the nozzle exit. Comparison between our ILES (black lines) and the experimental data of [6] (green lines). The orange lines correspond to a −5/3 slope.

experimental data show that for the round jet at the present regime ($M = 0.4$, $Re = 460,000$), the first five modes return the overall sound pressure level (OASPL) with an error of less than 1 dB, and the SPL with an error less than 1 dB/St up to $St = 2$, for all aft angles. Thirdly, selective far-field and compactness assumptions are made, taking advantage of a distant observer and a limited radial extent of the source, while retaining the phase lag along the non-compact axial extent, which is at the origin of the axisymmetric superdirectivity of subsonic round jets. This third assumption allows us to conduct one more direction of the volume integral prior to the acoustic computation, which reduces the latter's cost by one more dimension, turning it almost instantaneously with respect to the cost of the simulation.

The detailed derivation of the present line-source formulation [42,43] can be found in Appendix A. The most important formulae are given in the following section, before the numerical implementation is described.

3.1. Integral formulation

The far-field noise emitted by a radially compact, azimuthally decomposed source region is written, in the frequency domain considering only the first component of Lighthill's tensor, as:

$$
p'(R_o, \theta_o, \varphi_o = 0, \omega) \approx \sum_{m=1}^{+\infty} B_m(R_o, \theta_o, \omega) \int_{-\infty}^{+\infty} A \, \Re\left[t_{11}(Z_s, m, \omega)\right] dZ_s
$$
$$
+ B_0(R_o, \omega) \int_{-\infty}^{+\infty} A \, t_{11}(Z_s, 0, \omega) \, dZs + B_{0'}(R_o, \theta_o, \omega) \int_{-\infty}^{+\infty} A \, t_{11}(Z_s, 0', \omega) \, dZ_s \tag{3}
$$

where $(R_o, \theta_o, \varphi_o)$ is the observer position expressed in spherical coordinates centred on the jet axis at the exit of the nozzle, (Z_s, R_s, φ_s) is the source position expressed in cylindrical coordinates (e.g., $Z_s \equiv x \equiv R_o \cos\theta_o$), ω is the angular frequency, and $\Re$ denotes the real part. B_m is a frequency-dependent mode directivity factor given by

$$
B_m(R_o, \theta_o, \omega) = \frac{-i^m \, k^{m+2} \, \sin^m \theta_o}{2^m m!} \, e^{-ikR_o} \qquad \text{for } m \geq 1
$$
$$
B_0(R_o, \omega) = \frac{-k^2}{2} \, e^{-ikR_o} \tag{4}
$$
$$
B_{0'}(R_o, \theta_o, \omega) = \frac{k^4 \, \sin^2 \theta_o}{8} \, e^{-ikR_o}
$$

where $k = \omega/c_0$ is the wavenumber in the medium at rest. A is what remains from the Green function inside the source integral. It accounts for the geometrical decay to the observer and for the phase lag on the line-source and is given by

$$
A(R_o, \theta_o, Z_s, \omega) = \frac{(R_o \cos\theta_o - Z_s)^2 \, e^{-ik\left(\frac{Z_s^2}{2R_o} - Z_s \cos\theta_o\right)}}{\left(R_o^2 + Z_s^2 - 2R_o Z_s \cos\theta_o\right)^{3/2}} \tag{5}
$$

t_{11} is a radial integral of the mth azimuthal mode of the first component of the Lighthill tensor τ_{11} and is given by

$$t_{11}(Z_s, m, \omega) = \int\limits_0^{+\infty} \tau_{11}(Z_s, R_s, m, \omega)\, R_s^{m+1} \mathrm{d}R_s \tag{6}$$

for $m \geq 0$, and

$$t_{11}(Z_s, 0', \omega) = \int\limits_0^{+\infty} \tau_{11}(Z_s, R_s, 0, \omega)\, R_s^3\, \mathrm{d}R_s \tag{7}$$

All notations and conventions are explicitly introduced and explained in details in Appendix A. The integration, as well as the azimuthal mode extraction, are conducted prior to the acoustic computation, which is only based on a line-source quantity, radiating for several observers and frequencies. Since the integration and extraction commute with the Fourier transform, they can be conducted directly within the incompressible flow computation, thus drastically reducing the storage by four orders of magnitude with respect to 3D fields (if the number of mesh nodes is a few hundreds in the transverse directions y and z). However, as explained in section A.4 for the radial integration, this is accurate only as the quantity $St\, M \sin\theta_0 (R_s/D)$ goes to zero.

In the following, Eq. (3) is referred to as "formulation Z", meaning that no compactness assumption is made in the axial source extent with respect to the distance from the observer. Nevertheless, if $Z_s \ll R_0$, the radiation at low aft angles may be obtained using a reduction of A to

$$A_C(R_0, \theta_0, Z_s, \omega) = \frac{\cos^2\theta_0\, \mathrm{e}^{\mathrm{i}kZ_s \cos\theta_0}}{R_0} \tag{8}$$

Then, considering the $\sin^m\theta_0$ factor in B_m, the contribution of azimuthal modes $m \geq 1$, as well as the one from $0'$, can be neglected at low θ_0, and the acoustic pressure may be obtained by the following simplified expression

$$p'(R_0, \theta_0, \varphi_0 = 0, \omega) \underset{\theta_0 \to 0}{\sim} \frac{-k^2\, \mathrm{e}^{-\mathrm{i}kR_0}\, \cos^2\theta_0}{2R_0} \int\limits_{-\infty}^{+\infty} \mathrm{e}^{\mathrm{i}kZ_s \cos\theta_0}\, t_{11}(Z_s, 0, \omega)\, \mathrm{d}Zs \tag{9}$$

which was derived by [6]. It exhibits that the acoustic field in a given direction θ_0 at a given frequency $\omega = kc_0$ is determined by the amplitude of the wavenumber $k\cos\theta_0$ in the axial wavenumber spectrum of the excitation at this frequency. Equation (9) is referred to as "formulation C" in the following. It means that a compactness assumption is made on the axial source extent to the 0th order in the directivity factor and to the first order in the phase factor. One of the contributions of the present study is to investigate how strong such assumptions are and how small θ_0 should be for the error to be acceptable.

Note that expressions (3) and (9) are only valid in the observer's plane $\varphi_0 = 0$. It is achieved without loss of generality given the homogeneity of the acoustic field, and the azimuthal phase description can simply be recovered by multiplying each mode component by $\exp(\mathrm{i}m\varphi_0)$.

3.2. Numerical implementation

As specified heretofore, only the first component T_{11} is considered in the present study. The contribution of the other components is weak, but could be included in the process with neither conceptual nor numerical more obstacles. Consistently with the ILES, the incompressible, isothermal, inviscid form of the Lighthill source term is used, namely $T_{11} = \rho_0 u_x u_x$. The first step to apply the present acoustic methodology is to extract the azimuthal modes of the Lighthill source term. The velocity field is first interpolated from the Cartesian mesh to a polar mesh (R_s, φ_s). In the radial direction, the mesh step is the same as the one used in the Cartesian mesh in the lateral directions. In the azimuthal direction, the mesh step is dynamically adjusted according to R_s with either square meshes, namely $\mathrm{d}\varphi_s \approx \mathrm{d}R_s/R_s$, or with a number of mesh nodes in the azimuthal arc greater than $16m$, where m is the mode index. The smallest mesh step resulting from these two conditions is retained, so that the azimuthal variations of the field are accurately described. A third-order Lagrange interpolation procedure is applied with a four-point stencil in the lateral directions. Then, the azimuthal modes are computed using Eq. (24) and Simpson's rule.

The integration in the radial direction (6) (as well as the subsequent one along the jet axis) is then done using Simpson's rule too. Such interpolation and integration schemes are more appropriate than linear ones in the present context of ILES-based high-order schemes in order to reduce the discretization errors for the small scales. The line-source quantity is obtained from 640 velocity field snapshots with a signal length of $100D/U_c$, that is, a sampling Strouhal number of 6.4 and a frequency resolution of $0.01D/U_c$. Then the line-source data is transformed into the frequency domain using a standard Fast Fourier Transform routine and a Tukey window over 2.5% of the signal at each end. Finally, the truncation issue at the boundary of the line integral is fixed by a Gaussian weighting of the following form,
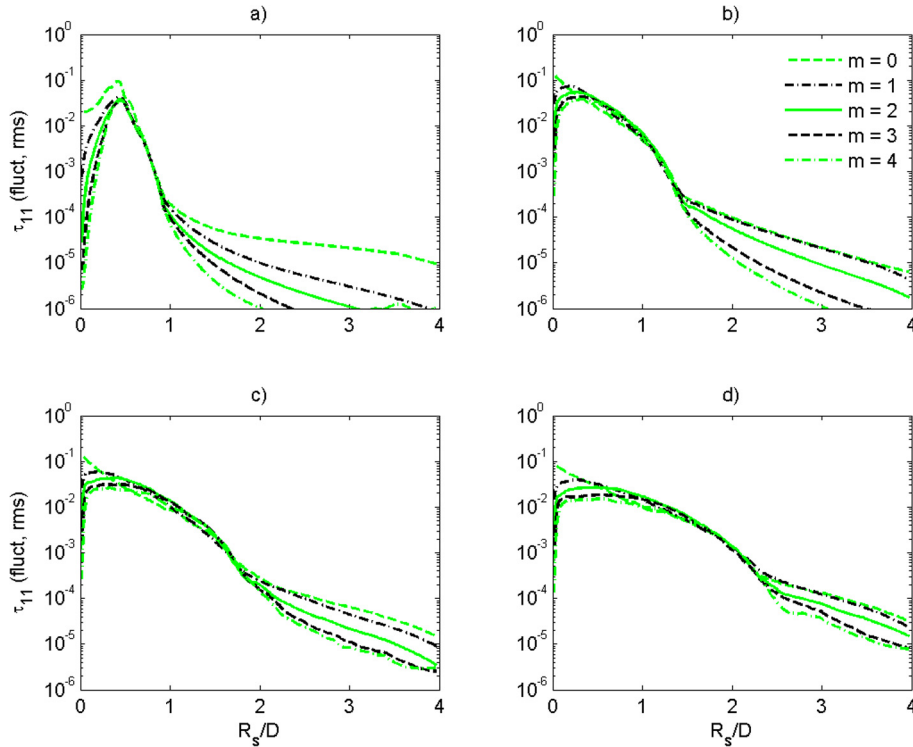
Fig. 5. Radial evolution of azimuthal modes (rms fluctuation): a) $Z_s/D = 2$, b) $Z_s/D = 6$, c) $Z_s/D = 10$, d) $Z_s/D = 14$. The unit is $\rho_0 U_c^2$.

$$w(Z_s) = e^{-\left(\dfrac{Z_s - \bar{Z}_s}{\Delta Z}\right)^4} \tag{10}$$

where $\bar{Z}_s$ is the end of the weighting, set to $9.5\,D$ and $0.2\,D$ at the outflow and inflow, respectively, while ΔZ is the pseudo-length, set to $7\,D$ and $0.5\,D$, respectively. Around these values, no significant influence of those parameters was noticed. The fourth-order Gaussian is preferred to the classical second-order one for its better smoothness near unity [44].

The observer locations in the plane $\varphi_0 = 0$ can be defined without any grid condition because they are totally independent of each other, contrary to some formulations of Lighthill's solution, transferring the space derivatives in the observer frame. Then, the same arc as in the experiment is used, with a better angular resolution enabling smoother plots.

In the present case, the line-source storage needs about 67 MB for five azimuthal modes (the storage of one component of the 3D, time-dependant velocity field requiring 1.5 TB, about $25,000$ times more), while the computation of expression (3) for about 20 observer points lasts a couple of seconds using an interpreted language on a standard desktop. Such a low storage and a low wall-clock time are very attractive features as far as a cost-efficient diagnostic tool is concerned. Moreover, robustness tests on the numerical parameters (distance from the observer, spectrum estimation, spatial windowing, quadrature formula, undersampling, etc.) can be conducted in a very comfortable way once the line-source distribution is known.

4. Acoustic results

In this section, the acoustic methodology presented above is applied using the velocity fields obtained by the ILES. Some visualisations during the source extraction process are first presented to check its suitability for the acoustic integral and to anticipate the behaviour of the latter. Then the radiated pressure field is compared to the experimental one.

4.1. Source field

The radial evolution of the five first azimuthal modes of the source quantity is plotted in Fig. 5 at four axial locations. Only the rms value of the modulus of the fluctuating part is considered. Note that the plot would be identical for $m < 0$ since, starting from real data, $\tau(-m) = \tau(m)^*$, where * denotes the complex conjugate, and $\tau(m = 0)$ is real. The spreading of the jet can be visualised, with a sharp maximum of fluctuation around $R_s/D \simeq 0.5$ close to the nozzle exit and a widening when approaching the axis for downstream locations. The five modes exhibit nearly the same evolution, with a Gaussian decay ($\sim e^{-R_s^2}$) followed by an exponential decay ($\sim e^{-|R_s|}$). They also have roughly the same energy in the shear region,
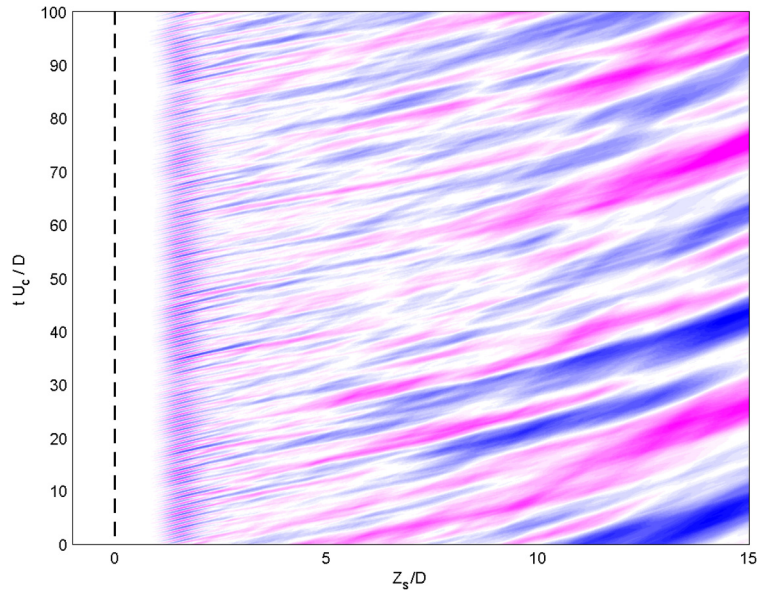
Fig. 6. Line-source spatio-temporal distribution for the axisymmetric mode ($m = 0$). The levels range from -0.02 (blue) to 0.02 (magenta). The unit is $\rho_0 U_c^2 D^2$. The thick, dashed, vertical line indicates the nozzle exit.

while on the axis or for high radii, the energy is decreasing for higher mode indexes. In the present context, the way the fluctuations are concentrated close to jet axis provides a first indication on the relevancy of the compactness assumption, driving the error made when taking the approximation of the Bessel function for small argument $St\, M \sin\theta_o (R_s/D)$, allowing one to take it out from the radial integral (28). Also, the streamwise velocity for $m \geq 1$ is theoretically expected to go to zero when approaching the centerline. Fig. 5 shows that the numerically extracted azimuthal modes satisfy well this necessary condition. Finally, given the low levels at high R_s, truncation effects due to the size of the computational box in the transverse directions are very unlikely.

The line-source distribution is mapped over the (Z_s, t) plane in Fig. 6 for the axisymmetric mode ($m = 0$). Fine-grained evolution is noticed for $0 \simeq Z_s/D \simeq 5$, with a convection velocity of about $0.6\,U_c$. Further downstream, the time and length scales of the fluctuations are growing, while the amplitude is greater, and the convection velocity slows down to about $0.35\,U_c$. The wavepacket formalism tells us that such subsonically convected waves are only able to radiate sound through the space and time modulation of their envelope. Indeed, the growth and decay rates of this envelope drive the amount of energy that will spill over the supersonic region of the axial wavenumber spectrum and will consequently be radiated to the far field [45–47]. Thus, the low-amplitude, fine-grained activity just downstream of the nozzle exit may be more efficient as a noise radiator than the high-amplitude, large-scale activity further downstream. Indeed, the growth of the large-scale activity occurs over a larger extent, with no real time modulation. Furthermore, its lower convection velocity pushes its energy peak away from the supersonic wavenumbers. On the contrary, the small-scale activity exhibits an alternation of bursts and relative quiet areas, as can be seen by following a $Z_s = 2D$ vertical line. Darker (high-level) spots are encountered around $t = [18; 35; 45; 55; 68; 90]D/U_c$. Due to the reduced size of the time series, only few events are happening, with intermittency, meaning that their acoustic imprint will not be optimally described in a spectrum estimation. This is one important limitation of the present study, yet it could be easily dealt with by extending the collection time of the data.

4.2. Radiated field

This line-source distribution is then used as the input for (3), and the acoustic pressure signal at the observer location is obtained on an arc at $R_o = 42\,D$. The resulting OASPL is plotted in Fig. 7 and compared with the experimental data. Regarding the latter, it can be checked in Fig. 7a that only the five first azimuthal modes are needed to describe the OASPL directivity with an error less than 1 dB, as mentioned in the introduction of section 3. Fig. 7a shows the main result of the paper: the present line-source formulation approaches the experimental OASPL by less than 4 dB for aft angles below $50°$. This is a noteworthy quantitative agreement, considering the important assumptions of the present formulation and its limitations (radial compactness, rather short collection time for the data and overprediction of the velocity fluctuations in the first stages of the jet development). An accurate prediction of the OASPL at higher aft angles would require to include other T_{ij}, in particular T_{22}, T_{23}, T_{33}, and to waive the compactness assumption in the radial direction. Also, the incompressible solver is unable to account for the refraction of the acoustic waves in the near-field, which can partly explain the slight overprediction of the OASPL at low aft angles.

Another valuable result from Fig. 7a is that the predicted directivity of the axisymmetric mode is in excellent qualitative agreement with the measured one. Moreover, the inclusion of the high-order formula (5) (formulation Z) for the
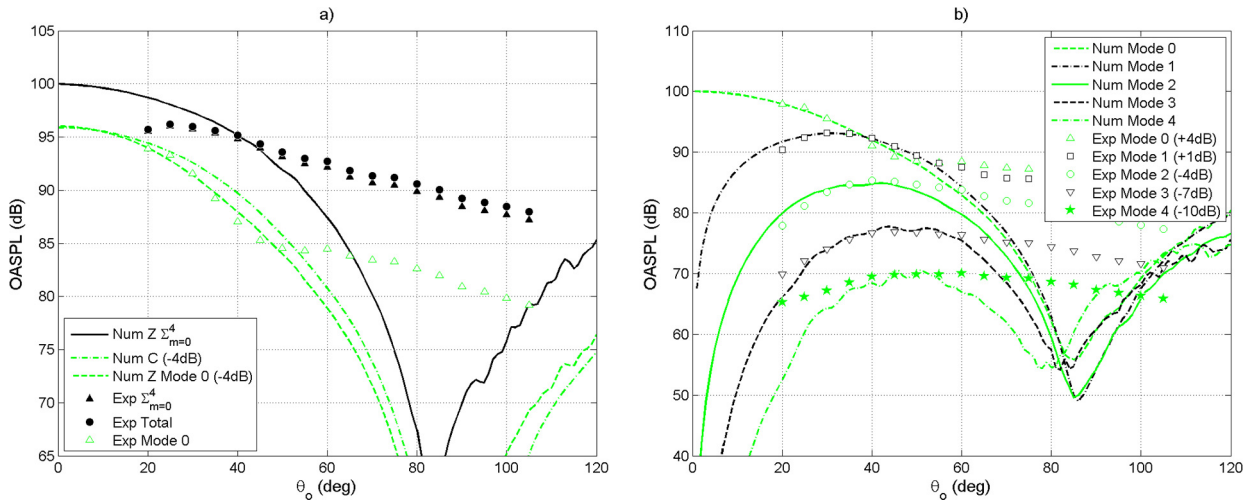
Fig. 7. Directivity. Left: total noise and axisymmetric mode; right: contributions of the five first azimutal Fourier modes. $R_o = 42D$.
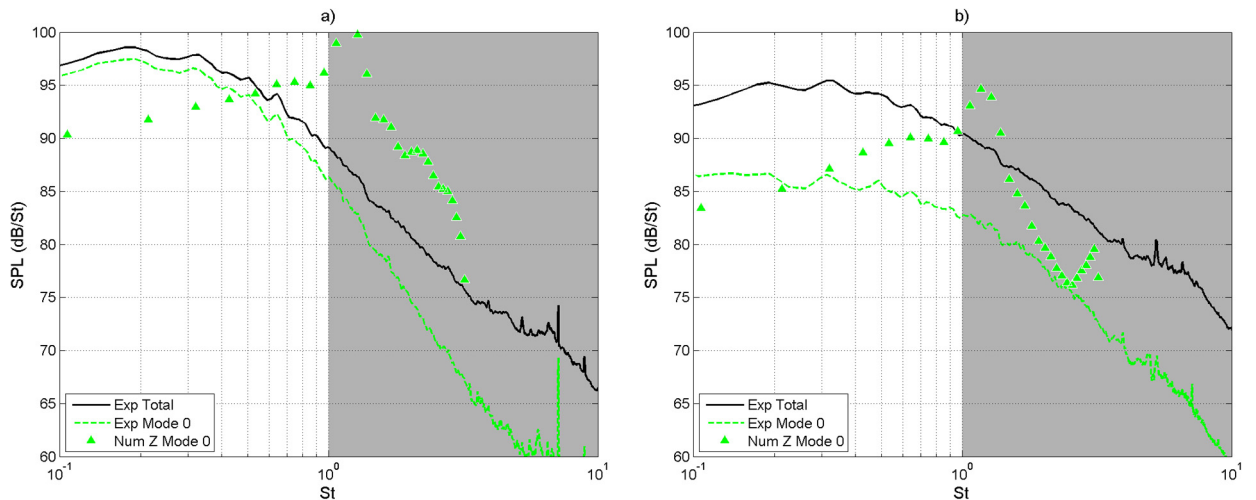

Fig. 8. Power spectral density for a) $\theta_0 = 20°$, b) $\theta_0 = 40°$. $R_o = 42\,D$. The greyed region ($St \geq 1$) corresponds to frequencies for which the line-source formulation is not valid.

geometrical decay to the observer and for the phase lag on the line-source is justified, since the more compact formula (8) (formulation C) leads to an underprediction of the energy fall in the moderate aft angles $20° \leq \theta_o \leq 50°$. Both formulations overestimate the OASPL of the axisymmetric mode by a 4-dB offset at low angles. This may be attributed to an amplification of the errors at high frequencies, as discussed at the end of this Section.

The directivity of the first azimuthal modes is also qualitatively well described by the present method at low aft angles, as shown in Fig. 7b. Two asymptotic behaviours are directly linked to the line-source formalism: for the first component of Lighthill's tensor (T_{11}), a $\cos^2 \theta_o$ factor, coming from A, weights all the azimuthal modes, leading to the cancellation of sound as θ_o approaches 90°. On the other hand, for $m \neq 0$, B_m introduces a $\sin^m \theta_o$ factor that vanishes the sound for small aft angles. This numerically predicted directivity agrees well with the experimental data for $20° \leq \theta_o \leq 60°$ for the four first modes. The radiation for θ_o approaching 90° may be attributed to the contribution of other T_{ij}. Such results suggest that the azimuthal mode decomposition has a physical meaning in the acoustic radiation processes of a turbulent jet. Including this decomposition into the present approach increases a priori its qualitative accuracy.

From a quantitative point of view, the OASPL of mode $m = 1$ is predicted with only a 1-dB error for $20° \leq \theta_o \leq 55°$. For the other modes, the energy hierarchy observed in the experiment is well recovered, but the OASPL needs a significant (from +4 dB to −10 dB) constant correction to match the experimental data. The k^{m+2} factor brought by B_m may explain those errors, since it reinforces strongly the high frequencies, which are, at the same time, the most concerned by the error made in assuming the quantity $St\,M\sin\theta_o(R_s/D)$ as small, as illustrated in Fig. 9.

Regarding the frequency content of the radiated noise, the power spectral density (PSD) of the pressure field is plotted in Figs. 8a and 8b for $\theta = 20°$ and $\theta = 40°$, respectively. For both observers, the SPL below $St = 1$ is consistent with the

previous observations: the error is of the same level as that for the OASPL. For very low frequencies, an underprediction is noticed, which may be attributed to the reduced size of the collection time for the present data. The increase of the SPL with frequencies corresponding to $St \leq 1$ can be attributed to two reasons. First, the acoustic pressure field is weighted by the factor k^2 (see Eq. (4)), inherited from the derivation of the Green function (see Eq. (17)). This affects the output of the acoustic model through errors in the numerical filtering of LES data brought by the Green function, which is fully analytical, would correctly cancel non propagating components of the source quantity. This is enhanced for higher-order modes, with extra powers of k inherited from the Bessel functions approximation for low arguments. Second, errors in the acoustic spectra could result from errors in the simulated velocity field. To determine whether such an error leads to over- or underestimation of the SPL would require unaffordable comparison between the LES and experimental spectra at each step of the construction of the line source, that is, T_{11}, its azimuthal modes, their radial integration.

The line-source formulation becomes theoretically wrong as long as the Strouhal number increases, as illustrated in Fig. 9. Experimental and theoretical studies about acoustic radiation from coherent structures in jets are usually limited to low Strouhal numbers (see [9] for instance, with no reported data for $St > 0.7$). That is why the spectral components for $St > 1$ are incorrect (as expected) and are not worth to be further discussed, except through the error they may yield in the overall SPL.

5. Concluding remarks

Including key elements of the jet noise radiation process such as the axial source extent and the decreasing efficiency of azimuthal modes, a cost-effective low-storage diagnostic tool could be designed and applied to a $Re = 460,000$, $M = 0.4$ round turbulent jet to predict the acoustic properties of the flow. The OASPL and the spectrum obtained in the present study compare fairly well with their experimental counterparts at low frequency and for moderate aft angles, without any empirical parameters. The present application has several limitations, which are summarised hereafter, with a discussion to see whether or not those limitations can be overcome.

- The agreement between the flow simulation and the experimental measurements is relatively good. Since the source quantity is based on the velocity field, this has a direct impact on the accuracy of the subsequent acoustic prediction. A finer tuning of the recycling technique may improve the quality of the velocity fields in the near field. Also, future studies will have to investigate the impact of our ILES strategy on the high-frequency content of the near field.
- The short collection time $(100 D/U_c)$ for this preliminary study prevents the amplitude modulation of the wavepackets to be well described by the signal processing. Since this is an important ingredient of the acoustic efficiency, a longer collection time should be considered. However, once the azimuthal mode extraction is integrated into the flow solver, this may not lead to storage issue.
- The major limitation of the methodology is the radial compactness assumption, which confines the correctness to low aft angles and low frequencies, namely $\theta_o \leq 50°$ and $St \leq 0.5$. Still, most of the acoustic power is produced there, thus this may be acceptable as a first quantitative estimation. The radial direction then appears as a controller for the accuracy of the solution for high θ_o and St. It is possible to reduce the azimuthal dynamics to a couple of azimuthal modes, while including the axial phase effects. Those in the radial direction could be included by waiving the compactness assumption, which would require a significant computational additional effort yet staying far below the cost of a full 3D integration.
- In the present study, only the first component of Lighthill's tensor was considered. This seems to be acceptable for low aft angles. Accuracy at high aft angles requires, in addition to radial phase effect, the inclusion of components that do not involve the streamwise direction, namely T_{22}, T_{33} and T_{23}, for T_{1j} formally vanishes at $\theta_o = 90°$.
- Finally, the ILES solves the incompressible Navier–Stokes equation. This is consistent with compactness assumptions. Nevertheless, it restricts the application of the present approach to low Mach numbers, since an analysis from linear parabolized stability equations showed that compressibility significantly reduces the growth rates of velocity fluctuations, in agreement with the streamwise evolution of measured amplitudes (see [9], figure 16). This may limit the accuracy of the acoustic prediction, even for low St and low polar angles. How low the Mach number should be remains an open question. The present value $M = 0.4$ appears to be low enough. Note that other Mach number values could be set in the acoustic part of the present method using the same (incompressible and non-dimensional) source data, for a negligible computational effort, as long as the compressibility and Reynolds number effects are not significant.

In a recent study by [21], eight Dielectric Barrier Discharge (DBD) plasma actuators located just before the nozzle exit were used as an active control device with the aim to enhance the mixing of a turbulent jet. Strong modifications of the vortex structures downstream of the nozzle exit, with a substantial reduction of the potential core, an increase of the jet radial expansion, and an improvement of the mixing properties of the flow were reported in this study performed with the exact same flow configuration. Thanks to the methodology presented in the present paper, the influence of the plasma actuators on the acoustic field will be investigated in a future study.

Acknowledgements

Appendix A. Line-source formalism

The full derivation of the line-source formulation [42,43] is given in this appendix. Starting with Lighthill's formalism, a far-field approximation is used to make the geometrical decay independent of the radial and azimuthal source position and to simplify the phase term. Then an azimuthal Fourier series expansion is used before a radial compactness is assumed, making the line-source quantity appears. The formalism is relatively similar to the one presented in [6], yet in the present approach, a less restrictive far-field assumption is taken. Finally, an a priori analysis of the error is deduced from the asymptotic behaviour of Bessel functions for small arguments.

A.1. Lighthill's integral solution

Taking the following Fourier transform

$$\mathcal{F}\left[\tilde{f}(\mathbf{x}, t)\right] = f(\mathbf{x}, \omega) = \int\limits_{-\infty}^{\infty} \tilde{f}(\mathbf{x}, t)\, \mathrm{e}^{-\mathrm{i}\omega t} \mathrm{d}t \tag{11}$$

where ω is the angular frequency and $\mathrm{i}^2 = -1$, the solution of the inhomogeneous Helmholtz equation

$$\left(\nabla^2 + k^2\right) p'(\mathbf{x}, \omega) = -S(\mathbf{x}, \omega) \tag{12}$$

where $k = \omega/c_0$ and c_0 is the speed of sound in the far-field, is given, in an unbounded medium at rest, by

$$p'(\mathbf{x}, \omega) = -\iiint\limits_{\mathcal{D}} S(\mathbf{y}, \omega)\, G(\mathbf{x}|\mathbf{y}, \omega)\, \mathrm{d}\mathbf{y} \tag{13}$$

where $\mathcal{D}$ is the source region and $\mathbf{y}$ the position in it, while $\mathbf{x}$ is the observer position. Using Lighthill's theory of aerodynamic noise, the source term S, which should vanish outside $\mathcal{D}$, is defined by

$$S = \frac{\partial^2 T_{ij}}{\partial y_i \partial y_j} = \frac{\partial^2}{\partial y_i \partial y_j}\left[\rho\, u_i\, u_j + (p' - c_\infty^2 \rho')\delta_{ij} + \sigma_{ij}\right] \tag{14}$$

where u_i are the components of the velocity field $\mathbf{u} = (u, v, w)$, ρ' is the density fluctuation from its value in the medium at rest and σ_{ij} stands for the components of the viscous stress tensor $\boldsymbol{\sigma}$. For low Mach numbers, isothermal, free shear flows, T_{ij} can be approximated [44] by $\rho_0 u_i u_j$, where ρ_0 is the supposed constant density of the fluid.

The Green function G corresponding to this problem is

$$G(\mathbf{x}|\mathbf{y}, \omega) = -\frac{\mathrm{e}^{-\mathrm{i}kr}}{4\pi r} \tag{15}$$

where $r = |\mathbf{x} - \mathbf{y}|$. The space derivatives in Eq. (14) can be transferred to G by virtue of the symmetry property of the convolution product. Thus they are exact, which is preferable than evaluating the derivatives from the numerical velocity fields. Since

$$\frac{\partial^2 G}{\partial y_i \partial y_j} = -\frac{\mathrm{e}^{-\mathrm{i}kr}}{r}\left[-k^2 \frac{r_i r_j}{r^2} + \frac{\mathrm{i}k}{r}\left(\frac{3r_i r_j}{r^2} - \delta_{ij}\right) + \frac{1}{r^2}\left(\frac{3r_i r_j}{r^2} - \delta_{ij}\right)\right] \tag{16}$$

with $r_i = x_i - y_i$ and δ_{ij} defined as the Kronecker's symbol, and by keeping only the $1/r$ term, expression (13) becomes

$$p'(\mathbf{x}, \omega) = -\frac{k^2}{4\pi} \iiint\limits_{\mathcal{D}} \frac{r_i r_j}{r^3} \mathrm{e}^{-\mathrm{i}kr}\; T_{ij}(\mathbf{y}, \omega)\, \mathrm{d}\mathbf{y} \tag{17}$$

A.2. Far-field assumption

Given the geometry of the round jet problem, it is relevant to write the observer location $\mathbf{x}$ in spherical coordinates $(R_o, \varphi_o, \theta_o)$ and the source location $\mathbf{y}$ in cylindrical coordinates (R_s, φ_s, Z_s), where R_o is the distance from the nozzle exit jet centre, φ is the azimuthal angle, while θ is the elevation angle with respect to the jet axis, along and from which the distances are Z_s and R_s, respectively. This yields:

$$r = \left[R_o^2 - 2R_o R_s \sin\theta_o \cos(\varphi_o - \varphi_s) - 2R_o Z_s \cos\theta_o + R_s^2 + Z_s^2 \right]^{\frac{1}{2}} \tag{18}$$

The source–observer distance r can be approximated at different degrees, according to far-field and compactness source assumptions. The least accurate option is to take

$$r \underset{|\mathbf{y}| \ll |\mathbf{x}|}{\sim} |\mathbf{x}| = R_o. \tag{19}$$

Neglecting R_s only leads to

$$r \underset{R_s \to 0}{\sim} \left[R_o^2 + Z_s^2 - 2R_o Z_s \cos\theta_o \right]^{\frac{1}{2}} \tag{20}$$

which may account for large axial source extent and small radial extent. As a reminder, Cavalieri et al. [6] used the following approximation

$$r \sim R_o - R_s \sin\theta_o \cos(\varphi_o - \varphi_s) - Z_s \cos\theta_o \tag{21}$$

Finally, neglecting $(R_s/R_o)^2$ and developing at first order the other terms than R_o^2 in Eq. (18) yields

$$r \sim R_o - R_s \sin\theta_o \cos(\varphi_o - \varphi_s) - Z_s \cos\theta_o + \frac{Z_s^2}{2R_o} \tag{22}$$

Here, expressions (22) and (20) are used for the phase term and the geometrical decay, respectively, in order to accurately take into account the axial distribution of the source. Then, considering only the component T_{11}, Eq. (17) becomes

$$p'(R_o, \varphi_o, \theta_o, \omega) \sim - \frac{k^2 e^{-ikR_o}}{4\pi} \int\limits_{-\infty}^{+\infty} \frac{(R_s \cos\theta_o - Z_s)^2 \, e^{-ik\left[\frac{Z_s^2}{2R_o} - Z_s \cos\theta_o \right]}}{\left[R_o^2 + Z_s^2 - 2R_o Z_s \cos\theta_o \right]^{1/2}}$$

$$\times \left[\int\limits_0^{+\infty} \int\limits_0^{2\pi} e^{ikR_s \sin\theta_o \cos(\varphi_o - \varphi_s)} T_{11}(R_s, \varphi_s, Z_s, \omega) \, d\varphi_s \, R_s \, dR_s \right] dZ_s \tag{23}$$

A.3. Azimuthal Fourier series expansion

One now can take advantage of the azimuthal homogeneity of the problem through an azimuthal Fourier series expansion of the source term. The azimuthal Fourier modes $\tau_{ij}(m)$ are thus introduced as

$$\tilde{\tau}_{ij}(Z_s, R_s, m, t) = \frac{1}{2\pi} \int\limits_0^{2\pi} \tilde{T}_{ij}(Zs, R_s, \varphi_s, t) \, e^{-im\varphi_s} d\varphi_s \tag{24}$$

which can be evaluated in the flow solver itself, replacing the storage of the fine azimuthal evolution of the source quantity by the storage of a given number of Fourier coefficients. The source tensor is then given by

$$\tilde{T}_{ij}(Z_s, R_s, \varphi_s, t) = \sum_{m=-\infty}^{+\infty} \tilde{\tau}_{ij}(Z_s, R_s, m, t) \, e^{im\varphi_s} \tag{25}$$

Reporting this into Eq. (23) yields

$$p'(R_o, \varphi_o, \theta_o, \omega) \sim - \frac{k^2 e^{-ikR_o}}{2} \int\limits_{-\infty}^{+\infty} A \int\limits_0^{+\infty} R_s$$

$$\sum_{m=-\infty}^{+\infty} \left(\tau_{11}(Z_s, R_s, m, \omega) \int\limits_0^{2\pi} e^{i[m\varphi_s + kR_s \sin\theta_o \cos(\varphi_o - \varphi_s)]} \frac{d\varphi_s}{2\pi} \right) dR_s \, dZ_s \tag{26}$$

where A is given by expression (5). The azimuthal integral can be rewritten as

$$\frac{e^{im\varphi_o}}{2\pi} \int_0^{2\pi} e^{i[m(\varphi_s-\varphi_o)+kR_s \sin\theta_o \cos(\varphi_s-\varphi_o)]} d\varphi_s = i^m\, e^{im\varphi_o}\, J_m(kR_s \sin\theta_o) \tag{27}$$

where J_m is the Bessel function of order m [48]. Then, a line quantity s_m can be defined as

$$s_m(Z_s,\omega) = \int_0^{\infty} \tau_{11}(Z_s,R_s,m,\omega)\, J_m(kR_s \sin\theta_o)\, R_s\, dR_s \tag{28}$$

Substitution into (26) leads to

$$p'(R_o,\varphi_o=0,\theta_o,\omega) \sim \sum_{m=-\infty}^{+\infty} \frac{-i^m\, k^2\, e^{-ikR_o}}{2} \int_{-\infty}^{+\infty} A\, s_m(Z_s,\omega)\, dZ_s \tag{29}$$

Note that for the physical analysis in the plane $\varphi_o = 0$, the out of phase modes (m and $-m$) are summed, and what is referred to as *mode m* is indeed $p'(m) + p'(-m)$. Moreover, starting from real data, $\tau_{11}(m=0)$ is real and $\tau_{11}(-m) = \tau_{11}(m)^*$, where $*$ denotes the complex conjugate. Consequently, since $J_{-m}(\xi) = (-1)^m J_m(\xi)$, it is possible to write $s_{-m} = (-1)^m s_m^*$. Combined with i^m from Eq. (27), it turns out finally that only the real part of T is involved in Eq. (3).

At this point, if the first azimuthal Fourier modes contain the main acoustic contribution, then the infinite discrete sum in expression (29) can reduce to a couple of 2D terms. With respect to the full 3D formulation (17), this saves a significant amount of source storage and computational cost. On the other hand, in the present form, the radial integration (28) must be evaluated for each frequency (through k) and for each observer elevation angle (θ_o). Assuming that the source is compact could reduce the problem by one more dimension, as presented in the following section. Source compactness is consistent with the use of incompressible data, which can successfully return the acoustic field for low Mach number cases [44,49].

A.4. Radial compactness

Using the asymptotic value of Bessel functions for small arguments [48], the dependency on R_s can be separated from the one on k and on θ_o. Indeed:

$$J_0(\xi) \underset{\xi\to 0}{\sim} \bar{J}_0(\xi) = 1 - \frac{\xi^2}{4} \quad , \qquad J_m(\xi) \underset{\xi\to 0}{\sim} \bar{J}_m(\xi) = \left(\frac{\xi}{2}\right)^m \frac{1}{m!} \quad (m \geq 1)$$

Then, Eq. (28) reduces to

$$s_m(Z_s,\omega) \underset{kR_s \sin\theta_o \to 0}{\sim} \frac{k^m \sin^m\theta_o}{2^m\, m!} \int_0^{\infty} \tau_{11}(Z_s,R_s,m,\omega)\, R_s^{m+1} dR_s \tag{30}$$

for $m \neq 0$ and

$$s_0(Z_s,\omega) \underset{kR_s \sin\theta_o \to 0}{\sim} \int_0^{\infty} \tau_{11}(Z_s,R_s,0,\omega)\, R_s\, dR_s$$

$$- \frac{k^2 \sin^2\theta_o}{4} \int_0^{\infty} \tau_{11}(Z_s,R_s,0,\omega)\, R_s^3\, dR_s \tag{31}$$

It means that the radial integration can be performed before the acoustic computation, while the front factor involving k and θ_o can be moved outside from the source integral. Reporting these into Eq. (29) leads to expression (3) and the definitions of B_m and t_{11} introduced in section 3.1.

The accuracy of the asymptotic values relies, however, on how small the product $kR_s \sin\theta_o$ is, which is a measure of the radial compactness, relatively to an observer elevation. The smaller θ_o is, the better it is. How small $kR_s \sin\theta_o$ is, not only determines whether the radial integration can be performed regardless of the observer, but also how J_{m+1} is smaller than J_m for a given small argument. That product is thus the most important parameter of the procedure. Before quantifying its influence on the accuracy of the Bessel function evaluation, consider that $\omega = 2\pi St\, U_c/D$, where St is the Strouhal number. Hence

$$kR_s \sin\theta_o = 2\pi St\, M \frac{R_s}{D} \sin\theta_o \tag{32}$$
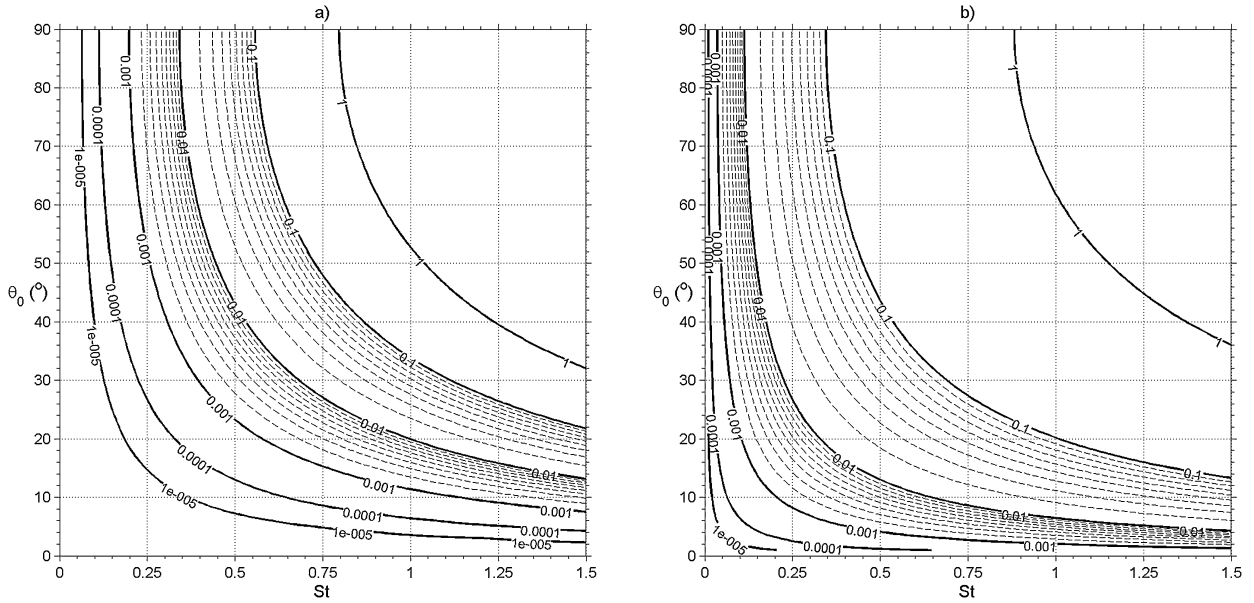
Fig. 9. Relative error of the asymptotic value of $J_m(\xi)$ for small argument $\xi = 2\pi\, St\, M\, \frac{R_s}{D}\sin\theta_o$ to the exact value, as a function of Strouhal number and observation elevation angle. Left: J_0, right: J_1. Case $M = 0.4$, $R_s/D = 1$.

The relative error of the asymptotic value of Bessel's functions $J_m(\xi)$ for small argument $\xi = kR_s\sin\theta_o$, noted $\bar{J}_m(\xi)$, is quantified here by $|J_m(\xi) - \bar{J}_m(\xi)|/|J_m(\xi)|$. The Mach number is fixed to 0.4, which is the value of the experimental data used in the present study for comparison, while the behaviour for other values can be directly deduced from the present results by expanding or contracting the Strouhal number scale accordingly. The latter is varied from 0 to 1.5, while only the first quarter of a circle can be considered for θ_o due to the symmetry of the argument.

Concerning R_s/D, a reasonable upper value is of the order of unity. Close to the nozzle exit, the shear occurs at around $R_s = D/2$ and it is spreading downstream. All in all, the radial extent over which the source quantity is significant should be considered.

Contour levels of the error corresponding to J_0 and J_1 are plotted in Figs. 9a) and 9b), respectively, for $R_s/D = 1$. The behaviour for other values of R_s/D can be directly deduced from the present results by expanding or contracting the Strouhal number scale accordingly. If an error of 10% is acceptable, for J_0, the radial compactness assumption is accurate up to $St = 0.55$ for all elevation angles, yet up to $St = 1.5$ for $\theta \leq 22°$ only. The range of validity for J_1 is qualitatively the same though significantly reduced.

Note that these conclusions are related to the error on the Bessel function evaluation, which has to be integrated over R_s. Thus, the global error of the procedure will depend on how the most efficient source components are distributed radially (if they are closer to the axis, the error will be small), combined with how they are distributed among the azimuthal modes and the Strouhal numbers (the lower, the better). Such distribution is more and more critical as θ_o is increasing.

References

[1] J. Bridges, C. Brown, Parametric testing of chevrons on single flow hot jets, in: 10th AIAA/CEAS Aeroacoustics Conference, 2004, p. 2824.
[2] R.L. Balzer, Segmented mixing device having chevrons for exhaust noise reduction in jet engines, September 2 2003, US Patent 6,612,106.
[3] G.A. Bres, V. Jaunet, M. Le Rallic, P. Jordan, T. Colonius, S.K. Lele, Large eddy simulation for jet noise: the importance of getting the boundary layer right, in: 21st AIAA/CEAS Aeroacoustics Conference, 2015, p. 2535.
[4] F. Kerhervé, P. Jordan, A.V.G. Cavalieri, J. Delville, C. Bogey, D. Juvé, Educing the source mechanism associated with downstream radiation in subsonic jets, J. Fluid Mech. 710 (2012) 606.
[5] P. Jordan, T. Colonius, Wave packets and turbulent jet noise, Annu. Rev. Fluid Mech. 45 (2013) 173–195.
[6] A.V.G. Cavalieri, P. Jordan, T. Colonius, Y. Gervais, Axisymmetric superdirectivity in subsonic jets, J. Fluid Mech. 704 (2012) 388–420.
[7] P.K. Ray, L.C. Cheung, S.K. Lele, On the growth and propagation of linear instability waves in compressible turbulent jets, Phys. Fluids 21 (5) (2009) 054106.
[8] D.G. Crighton, P. Huerre, Shear-layer pressure fluctuations and superdirective acoustic sources, J. Fluid Mech. 220 (1990) 355–368.
[9] A.V.G. Cavalieri, D. Rodriguez, P. Jordan, T. Colonius, Y. Gervais, Wavepackets in the velocity field of turbulent jets, J. Fluid Mech. 730 (2013) 559–592.
[10] V. Jaunet, P. Jordan, A.V.G. Cavalieri, Two-point coherence of wave packets in turbulent jets, Phys. Rev. Fluids 2 (2) (2017) 024604.
[11] S. Piantanida, V. Jaunet, J. Huber, W.R. Wolf, P. Jordan, A.V.G. Cavalieri, Scattering of turbulent-jet wavepackets by a swept trailing edge, J. Acoust. Soc. Amer. 140 (6) (2016) 4350–4359.
[12] A.G. Kravchenko, P. Moin, On the effect of numerical errors in large eddy simulation of turbulent flows, J. Comput. Phys. 131 (1997) 310–322.
[13] R. Gautier, S. Laizet, E. Lamballais, A DNS study of jet control with microjets using an immersed boundary method, Int. J. Comput. Fluid Dyn. 28 (6–10) (2014) 393–410.
[14] S.K. Lele, Compact finite difference schemes with spectral-like resolution, J. Comput. Phys. 103 (1992) 16–42.

[15] S. Laizet, E. Lamballais, High-order compact schemes for incompressible flows: a simple and efficient method with the quasi-spectral accuracy, J. Comput. Phys. 228 (16) (2009) 5989–6015.

[16] S. Laizet, N. Li, Incompact3d, a powerful tool to tackle turbulence problems with up to $O(10^5)$ computational cores, Int. J. Numer. Methods Fluids 67 (11) (2011) 1735–1757.

[17] S. Laizet, J.C. Vassilicos, Stirring and scalar transfer by grid-generated turbulence in the presence of a mean scalar gradient, J. Fluid Mech. 764 (2015) 52–75.

[18] L.F.R. Espath, L.C. Pinto, S. Laizet, J.H. Silvestrini, High-fidelity simulations of the lobe-and-cleft structures and the deposition map in particle-driven gravity currents, Phys. Fluids 27 (5) (2015) 056604.

[19] C. Diaz Daniel, S. Laizet, J.C. Vassilicos, Direct numerical simulation of the interaction between a turbulent boundary layer and a wall-attached cube, Phys. Fluids 29 (2017) 055102.

[20] T. Dairay, V. Fortuné, E. Lamballais, L.E. Brizzi, LES of a turbulent jet impinging on a heated wall using high-order numerical schemes, Int. J. Heat Fluid Flow 50 (2014) 177–187.

[21] V. Ioannou, S. Laizet, Numerical investigation of plasma-controlled turbulent jets for mixing enhancement, Int. J. Heat Fluid Flow 70 (2018) 193–205.

[22] O. Mahfose, S. Laizet, Skin-friction drag reduction in a channel flow with streamwise-aligned plasma actuators, Int. J. Heat Fluid Flow 66 (2017) 83–94.

[23] T.S. Lund, X. Wu, K.D. Squires, Generation of turbulent inflow data for spatially-developing boundary layer simulations, J. Comput. Phys. 140 (2) (1998) 233–258.

[24] J. Nordström, N. Nordin, D. Henningson, The fringe region technique and the Fourier method used in the direct numerical simulation of spatially evolving viscous flows, SIAM J. Sci. Comput. 20 (4) (1999) 1365–1393.

[25] J. Craske, M. van Reeuwijk, Robust and accurate open boundary conditions for incompressible turbulent jets and plumes, Comput. Fluids 86 (2013) 284–297.

[26] N. Hasan, S.F. Anwer, S. Sanghi, On the outflow boundary condition for external incompressible flows: a new approach, J. Comput. Phys. 206 (2005) 661–683.

[27] E. Lamballais, V. Fortuné, S. Laizet, Straightforward high-order numerical dissipation via the viscous term for direct and large eddy simulation, J. Comput. Phys. 230 (2011) 3270–3275.

[28] T. Dairay, E. Lamballais, S. Laizet, J.C. Vassilicos, Numerical dissipation vs. subgrid-scale modelling for large eddy simulation, J. Comput. Phys. 337 (2017) 252–274.

[29] E. Tadmor, Convergence of spectral methods for nonlinear conservation laws, SIAM J. Numer. Anal. 26 (1) (1989) 30–44.

[30] G.S. Karamanos, G.E. Karniadakis, A spectral vanishing viscosity method for large-eddy simulations, J. Comput. Phys. 163 (1) (2000) 22–50.

[31] A.K.M. Fazle Hussain, K.B.M.Q. Zaman, The "preferred mode" of the axisymmetric jet, J. Fluid Mech. 110 (1981) 39–71.

[32] C.-M. Ho, P. Huerre, Perturbed free shear layers, Annu. Rev. Fluid Mech. 16 (1) (1984) 365–422.

[33] M.J. Lighthill, On sound generated aerodynamically. I. General theory, Proc. R. Soc. A 223 (1952) 1–32.

[34] F. Bastin, P. Lafon, S. Candel, Computation of jet mixing noise due to coherent structures: the plane jet case, J. Fluid Mech. 335 (1) (1997) 261–304.

[35] J.B. Freund, Noise sources in a low-Reynolds-number turbulent jet at Mach 0.9, J. Fluid Mech. 438 (2001) 277.

[36] D.J. Bodony, S.K. Lele, Low-frequency sound sources in high-speed turbulent jets, J. Fluid Mech. 617 (2008) 231.

[37] F. Margnat, V. Fortuné, An iterative algorithm for computing aeroacoustic integrals with application to the analysis of free shear flow noise, J. Acoust. Soc. Amer. 128 (4) (2010) 1656–1667.

[38] C. Moser, E. Lamballais, F. Margnat, V. Fortuné, Y. Gervais, Numerical study of Mach number and thermal effects on sound radiation by a mixing layer, Int. J. Aeroacoust. 11 (5–6) (2012) 555–580.

[39] Alfons Michalke, A Wave Model for Sound Generation in Circular Jets, 1970.

[40] A. Michalke, H.V. Fuchs, On turbulence and noise of an axisymmetric shear flow, J. Fluid Mech. 70 (1) (1975) 179–205.

[41] J.B. Freund, Noise-source turbulence statistics and the noise from a Mach 0.9 jet, Phys. Fluids 15 (6) (2003) 1788–1799.

[42] S.C. Crow, Acoustic gain of a turbulent jet, in: Paper IE.6, Meeting of Division of Fluid Dynamics, American Physical Society, University of Colorado, Boulder, CA, USA, November 1972, 1972.

[43] J.E.F. Williams, A.J. Kempton, The noise from the large-scale structure of a jet, J. Fluid Mech. 84 (4) (1978) 673–694.

[44] F. Margnat, X. Gloerfelt, On compressibility assumptions in aeroacoustic integrals: a numerical study with subsonic mixing layers, J. Acoust. Soc. Amer. 135 (2014) 3252–3263.

[45] D. Obrist, Directivity of acoustic emissions from wave packets to the far field, J. Fluid Mech. 640 (2009) 165–186.

[46] A.V.G. Cavalieri, P. Jordan, A. Agarwal, Y. Gervais, Jittering wavepacket models for subsonic jet noise, J. Sound Vib. 330 (2011) 4474–4492.

[47] R. Serré, J.-C. Robinet, F. Margnat, The influence of a pressure wavepacket's characteristics on its acoustic radiation, J. Acoust. Soc. Amer. 137 (4) (2015) 3178–3189.

[48] M. Abramovitz, I.A. Stegun, Handbook of Mathematical Functions, Dover, New York, 1965.

[49] F. Margnat, Hybrid prediction of the aerodynamic noise radiated by a rectangular cylinder at incidence, Comput. Fluids 109 (4) (2015) 13–26.